PERGAMON

International Journal of Heat and Mass Transfer 44 (2001) 3413–3429

International Journal of HEAT and MASS TRANSFER

www.elsevier.com/locate/ijhmt

A conservation-based discretization approach for conjugate heat transfer calculations in hot-gas ducting turbomachinery components

E. Papanicolaou *, D. Giebert, R. Koch, A. Schulz

Institut für Thermische Strömungsmaschinen, Universität Karlsruhe (TH), Karlsruhe, Germany

Received 1 August 2000; received in revised form 1 December 2000

Abstract

A numerical procedure has been developed for simulation of conjugate heat transfer in generalized coordinates and used in some typical turbomachinery applications. Discretized equations for nodes located exactly on the solid–fluid interface were derived using energy conservation principles, yielding the corresponding temperatures directly, without the need for inter- or extrapolation from adjacent nodes. A finite-volume-based computer code was used along with the SIMPLE algorithm and the k–ϵ turbulence model. The turbulent flow and heat transfer in a stepped labyrinth seal and in an effusion-cooled combustor liner have been studied and results were compared with measured data showing good agreement. In the labyrinth-seal case, the comparisons were in terms of surface temperatures and Nusselt numbers, while for the effusion-cooling case in terms of the streamwise velocity and the film-cooling effectiveness for different blowing and density ratios. In the latter case, two different liner materials were used to study the influence of the thermal conductivity on film-cooling characteristics and the agreement was better for the lowest of the two conductivities. The dominant flow structures could be captured with good accuracy.

1. Introduction

In several industrial applications it is necessary to accompany the computation of the flow and associated heat transfer in the fluid with the heat conduction inside the adjacent solid surfaces. The coupling of these two modes of heat transfer has been identified by the name 'conjugate heat transfer' in the literature. Typical applications where conjugate heat transfer effects can be important are, among others, the cooling of turbine blades [1] and the cooling of electronics [2]. It is therefore important to incorporate in existing computational fluid dynamics (CFD) codes an appropriate scheme for coupled heat transfer computations, capable of handling complex geometries.

Kelkar et al. [3] have carried out conjugate heat transfer computations in boundary-fitted coordinates by using an 'effective conductance' to define the interface conductivity between the solid and the fluid regions. This was an extended form of the 'harmonic mean' approach, proposed by Patankar [4] for Cartesian grids, in non-orthogonal coordinates. As test problems, the conduction in a composite slab, natural convection between eccentric tubes and forced convection over an array of cylinders were considered. Bohn and Bonhoff [5] applied a conjugate heat transfer method to compute the transonic flow and heat transfer over a turbine blade with coolant injection on the suction side. Differences between computations not accounting for and those that do account for heat transfer in the blade were compared and the impact of the latter, more realistic computations on the design of such a blade were analyzed. Three-dimensional results for a similar configuration were also presented by Bohn et al. [6]. The coolant was injected

* Corresponding author. Present address: "Demokritos" National Center for Scientific Research, Solar and Other Energy Systems Laboratory, Aghia Paraskevi, 15310 Attiki, Greece. Tel.: +30-1-650-3817; fax: +30-1-654-4592.

E-mail address: elpapa@mail.demokritos.gr (E. Papanicolaou).

0017-9310/01/$ - see front matter
PII: S0017-9310(01)00017-5

Nomenclature

a_{ij}	cofactor in the coordinate transformation (Jacobian) matrix: $a_{ij} = \partial x_i/\partial \xi_j$
b	thickness of labyrinth fins
C_D	discharge coefficient $C_D = \dot{m}/\dot{m}_{id}$
C_p	specific heat at constant pressure (J/kg K)
h	enthalpy of the fluid
H_s	height of the steps in stepped-labyrinth seals
J	Jacobian of the coordinate transformation matrix, defined as $J = \mid \partial x_i/\partial \xi_j \mid$
k	turbulent kinetic energy
$\dot{m}$	mass flow rate (kg/s)
M	blowing ratio in the film-cooling application $M = (\rho u)_c/(\rho u)_m$
Ma	Mach number
Nu	mean Nusselt number $Nu = \alpha 2s/\lambda_f$
p	static pressure
Pr	Prandtl number $Pr = \mu C_p/\lambda$
Re	Reynolds number in the labyrinth seal flow $Re = 2\dot{m}/\mu w$
s	clearance of the labyrinth seals
T	static temperature
u_j	Cartesian velocity component
U_j	velocity component in the transformed coordinates $U_j = u_k a_{kj}$
w	depth of the labyrinth flow channel

Greek symbols

α	heat transfer coefficient (W/m^2 K)
ϵ	rate of dissipation of turbulent kinetic energy
ξ, η, ζ (or ξ_j)	coordinates in the curvilinear (transformed) system
λ	thermal conductivity (W/m K)
μ	molecular viscosity (Ns/m)
μ_t	turbulent viscosity
ρ	density (kg/m^3)

Subscripts

c	coolant flow
ex	exit values
f	fluid domain
id	ideal
m	main flow in the film-cooling problem
o	total (stagnation) quantities
s	solid domain

from a row of holes and different angles of incidence of the hot gas flow were considered. In another study by Bohn et al. [1], computations were carried out for a film-cooled blade with injection holes at the leading edge, showing that conjugate heat transfer may also affect the aerodynamics of the cooling jets. The cooling of turbine blades was also the subject of the work of Heselhaus and Vogel [7]. They presented a coupled scheme between a finite-volume-based Navier–Stokes solver and a finite-element-based program for heat conduction and used it to compute the flow over a turbine stator blade with internal cooling. The latter was achieved through three internal cooling channels. The numerical procedure was based on an iterative procedure, whereby at each step heat fluxes arising from the computation of the flow and convective heat transfer were used as boundary conditions for the computation of heat conduction inside the blade walls. Finally, an effusion-cooling problem has recently been presented by Bohn and Moritz [8].

In the present study, a procedure for treating the implicit coupling between convection in the fluid and conduction in adjacent solid surfaces is being presented, implemented in three dimensions and for body-fitted coordinates. For the selected control-volume-based computer code, the methodology proposed is very suitable, as it is based exclusively on conservation principles. As a first representative application from the field of turbomachinery where conjugate heat transfer is of importance, the flow inside labyrinth seals was studied. There are a number of investigations on this topic, both by experimental and numerical methods including compressibility and rotational effects and these will be reviewed in a later section. The current work is a step ahead compared to the previous studies of labyrinth seals, by using body-fitted coordinates, a more systematic procedure to deal with the coupling between fluid and solid heat transfer and the use of a turbulence model which is better suited to recirculating flows with heat transfer. In addition, a representative problem from the area of cooling of turbomachinery components is also investigated. The analysis of an effusion-cooled combustor liner, where conjugate heat transfer effects are essential for determining the cooling requirements.

2. Mathematical model

2.1. Model equations

In a three-dimensional, Cartesian coordinate system, the steady, incompressible flow equations for a gas which is thermodynamically ideal, as assumed in this study, can be described by the following time-averaged equations of turbulent mass, momentum and energy transport:

$$\frac{\partial \overline{u}_i}{\partial x_i} = 0, \tag{1}$$

$$\rho \overline{u}_i \frac{\partial \overline{u}_j}{\partial x_i} = -\frac{\partial \overline{p}}{\partial x_j} + \frac{\partial}{\partial x_i}\left[\mu\left(\frac{\partial \overline{u}_j}{\partial x_i} + \frac{\partial \overline{u}_i}{\partial x_j}\right) - \rho\overline{u_i' u_j'}\right], \tag{2}$$

$$\rho \overline{u}_i \frac{\partial \overline{h}}{\partial x_i} = \frac{\partial}{\partial x_i}\left(\frac{\mu}{Pr}\frac{\partial \overline{h}}{\partial x_i} - \rho\overline{u_i' h'}\right), \tag{3}$$

where the overbars denote mean quantities. The Reynolds stress terms and the turbulent heat fluxes, following the Bousinessq eddy viscosity concept, can be written as:

$$-\rho\overline{u_i' u_j'} = \mu_t\left(\frac{\partial \overline{u}_j}{\partial x_i} + \frac{\partial \overline{u}_i}{\partial x_j}\right) - \frac{2}{3}\rho k \delta_{ij} \quad \text{and}$$

$$-\rho\overline{u_i' h'} = \frac{\mu_t}{Pr_t}\left(\frac{\partial h}{\partial x_i}\right). \tag{4}$$

For the k–ϵ model, which is used in the present study, the transport equations for k and ϵ are given by

$$\rho \overline{u}_i \frac{\partial k}{\partial x_i} = \frac{\partial}{\partial x_i}\left[\left(\mu + \frac{\mu_t}{\sigma_k}\right)\frac{\partial k}{\partial x_i}\right] + P_k - \rho\epsilon, \tag{5}$$

$$\rho \overline{u}_i \frac{\partial \epsilon}{\partial x_i} = \frac{\partial}{\partial x_i}\left[\left(\mu + \frac{\mu_t}{\sigma_\epsilon}\right)\frac{\partial \epsilon}{\partial x_i}\right] + (C_1 f_1 P_k - \rho C_2 f_2 \epsilon)\frac{\epsilon}{k} + E, \tag{6}$$

where the turbulent viscosity μ_t and the production term P_k of the turbulent kinetic energy are obtained from the following expressions:

$$\mu_t = \rho f_\mu C_\mu \frac{k^2}{\epsilon}, \quad P_k = \left[\mu_t\left(\frac{\partial \overline{u}_j}{\partial x_i} + \frac{\partial \overline{u}_i}{\partial x_j}\right) - \frac{2}{3}\rho k \delta_{ij}\right]\frac{\partial \overline{u}_j}{\partial x_i}. \tag{7}$$

The constants have typically the following values: $C_\mu = 0.09$, $C_1 = 1.44$, $C_2 = 1.92$, $\sigma_k = 1.0$ and $\sigma_\epsilon = 1.3$. The damping functions f_μ, f_1, f_2 are equal to 1 in the standard k–ϵ model and the term E, which accounts for low-Reynolds number effects in the vicinity of the wall is equal to 0. In this work, both a low-Reynolds model as well as the standard k–ϵ turbulence model [9] with the wall function approach [9,10] have been used to model turbulence effects. The low-Reynolds model of Abe et al. [11] was used for the computation of labyrinth seals (AKN model) and the standard k–ϵ in the effusion cooling problem, which required a significantly higher number of grid points. The AKN model is particularly well suited for recirculating flows that are expected to develop in such configurations, since it employs the Kolmogorov velocity scale u_ϵ instead of the commonly used friction velocity u_τ, which is subject to singularities at separation and reattachment points. In the AKN model the following equations are used:

$$u_\epsilon = (\nu\epsilon)^{1/4}, \quad y^* = \frac{u_\epsilon y}{\nu}, \quad R_t = \frac{k^2}{\nu\epsilon}, \tag{8}$$

$$f_\mu = \left\{1 - \exp\left(-\frac{y^*}{14}\right)\right\}^2\left[1 + \frac{5}{R_t^{3/4}}\exp\left\{-\left(\frac{R_t}{200}\right)^2\right\}\right], \tag{9}$$

$$f_\epsilon = \left\{1 - \exp\left(-\frac{y^*}{3.1}\right)\right\}^2\left[1 - 0.3\exp\left\{-\left(\frac{R_t}{6.5}\right)^2\right\}\right], \tag{10}$$

while at the wall the value for ϵ is specified by

$$\epsilon_w = 2\nu\left(\frac{\partial\sqrt{k}}{\partial n}\right) = 2\nu\frac{k_1}{n_1^2},$$

where k_1, n_1 are the values of k and the wall distance at the first point from the wall. The model constants are also different and more specifically: $C_\mu = 0.09$, $C_1 = 1.5$, $C_2 = 1.9$, $\sigma_k = 1.4$, $\sigma_\epsilon = 1.4$, $E = 0$. The turbulent Prandtl number is taken as constant throughout this study ($Pr_t = 0.86$). Thus, the closure problem reduces to the specification of the turbulent viscosity for momentum.

After transforming into generalized coordinates, the transport Eqs. (1)–(3), can be written in conservative form in terms of a generic variable ϕ

$$\frac{\partial}{\partial \xi_j}(\rho U_j \phi) = \frac{\partial}{\partial \xi_j}\left[\frac{\Gamma}{J}\left(q_{jm}\frac{\partial \phi}{\partial \xi_m}\right)\right] + J \cdot s(\xi_j), \tag{11}$$

where $q_{jm} = a_{1j}a_{1m} + a_{2j}a_{2m} + a_{3j}a_{3m}$. The as are the cofactors of the Jacobian matrix in the coordinate transformation [10] and Γ the diffusion coefficient.

3. Computational scheme

3.1. Main features

The computer code used for the present simulations was developed at the "Institut für Thermische Strömungsmaschinen" of the University of Karlsruhe. It has been tested in a variety of flow problems, such as, for instance, those studied by Benz et al. [12], Giebert et al. [13,14]. The discretized Navier–Stokes equations are solved along with suitable turbulence models on body-fitted, non-orthogonal curvilinear coordinate systems. A fully conservative, structured finite-volume discretization method is employed. The SIMPLE algorithm of Patankar and Spalding [15] is used for solving the pressure-correction equation along with the momentum equations in an iterative solution procedure. A non-staggered grid is employed along with the momentum-interpolation procedure of Rhie and Chow [16], to avoid the checkerboard-splitting problem with the pressure.

The diffusive terms are discretized by a second-order central differencing scheme, whereas for the convective terms of all transport equations the second-order accurate, bounded monotonized-linear-upwind scheme (MLU) [17] is used. Because of its good stability, this higher-order scheme can be used for the discretization of the convective terms of the turbulence equations (Eqs. (5) and (6)) as well. A generalized conjugate gradient iterative procedure, with an incomplete lower-upper decomposition (ILU-CG [18]) is used to solve the system of the algebraic equations arising from the discretization. Various other iterative solvers have been implemented in the present code (SIP [19], BiCGSTAB [20]) but the ILU-CG solver has been selected here due to its performance in terms of effectiveness, robustness and computing time.

3.2. Treatment of the solid–fluid coupling conditions

For the enthalpy, the generic symbols in Eq. (11) are:

$$\phi = h, \quad \Gamma = \frac{\mu}{Pr} + \frac{\mu_t}{Pr_t}.$$

Thus, the discretized form of the enthalpy equation is

$$\frac{\partial I_\xi}{\partial \xi} + \frac{\partial I_\eta}{\partial \eta} + \frac{\partial I_\zeta}{\partial \zeta} = s_{cd} + J \cdot s(\xi, \eta, \zeta),$$

where the symbol I denotes the total, convective plus diffusive flux and s are the local source terms. By integrating over the control volumes it takes the following form:

$$\int_{\Delta V} \frac{\partial I_\xi}{\partial \xi} \mathrm{d}V + \int_{\Delta V} \frac{\partial I_\eta}{\partial \eta} \mathrm{d}V + \int_{\Delta V} \frac{\partial I_\zeta}{\partial \zeta} \mathrm{d}V = \underbrace{\int_{\Delta V} s_{cd} \, \mathrm{d}V}_{S_{cd}} + \underbrace{\int_{\Delta V} J \cdot s(\xi, \eta, \zeta) \, \mathrm{d}V}_{S} \tag{12}$$

The integrated source terms on the right-hand side consist of the cross-diffusion contribution, S_{cd}, and possibly the pressure work and dissipation as well, depending on whether the latter two are important enough to be considered or not. For the control volumes that are located entirely inside the fluid or the solid domains, the integration proceeds straightforward [10]. For the treatment of the coupling of the heat transfer between the fluid and solid domains, a discretization procedure that somewhat differs from previous studies is adopted, which will be briefly described subsequently.

The main idea has already been outlined in a previous study by Papanicolaou and Jaluria [2], where the discretized equations were presented for Cartesian coordinates and here an extended form for generalized coordinates is presented. Nodes are placed on the solid–fluid interface, yielding the interface temperature directly as part of the solution. These nodes are treated as boundary nodes for the computation of the flow while for the enthalpy equation, regular control volumes are needed in that location, through which the coupling will be achieved. Therefore, the enthalpy equation is solved over a grid which is slightly modified in the vicinity of the solid–fluid interface. To form these special control volumes an auxiliary grid line is created at a distance from the wall of 1/4 of the width of the cell adjacent to the wall in the fluid region (see Fig. 1). For simplicity, the first grid line inside the solid is placed at the same distance from the solid-fluid boundary in Fig. 1. This process, in three-dimensional configurations, generates surfaces parallel to the solid–fluid interface on either side

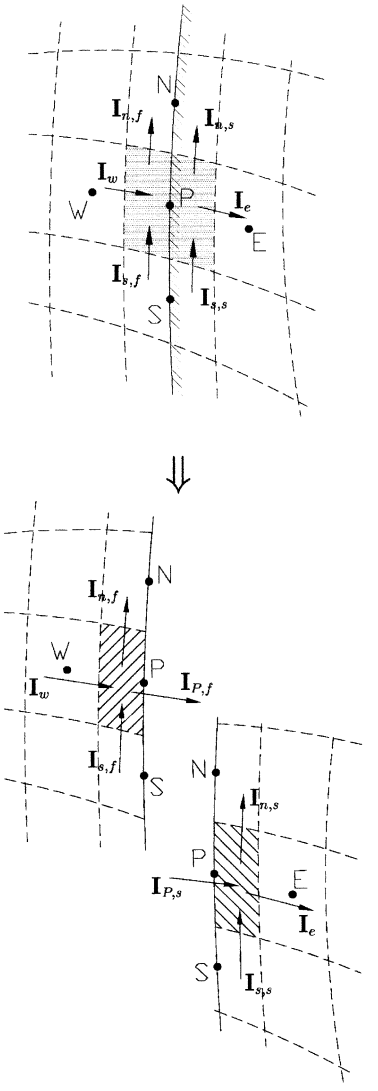

Fig. 1. A typical interface control volume and the splitting approach. The shaded control volume on the fluid side (left) is formed by adding a new face halfway between points P and W.

of it and control volumes which lie partly in the solid and partly in the fluid region. With such an arrangement, the computation of transport variables that are needed on the control volume face on the fluid side is facilitated, as this face is located midway between nodes.

As shown in Fig. 1, from these original control volumes on the solid–fluid interface, one may imagine for a moment a splitting procedure by means of which two separate control volumes ΔV_f and ΔV_s are formed. In each of these, the energy balance is performed as for any other control volume, according to Eq. (12), leaving the enthalpy flux at each side of the common interface as an unknown. The expressions that arise for this unknown flux from the energy balance are made equal to each other (Appendix A) and a discretized enthalpy equation is thus obtained for the interface nodes, which are associated with the now recombined full control volumes. With this treatment, the coupling between the solid and fluid regions is achieved not only through points in the direction normal to the interface, but through all adjacent points, i.e., lateral diffusion effects are also taken into account and one dimensionality is not assumed. In addition, this practice is more consistent with the control-volume approach, as it is based on conservation principles, rather than a direct discretization of the derivatives involved in the heat flux, which, in addition, would have resulted in forward or backward difference approximations, whereas, with the present approximation, heat fluxes are made equal exactly on the interface.

3.3. Validation – flat plate of finite thickness

In order to asses the proposed scheme with respect to handling the thermal boundary condition on the fluid–solid interface, suitable test cases from the literature were sought. As such, the laminar flow over a flat plate with conjugate heat transfer was selected, for which several analytical solutions are available. The mathematical approaches seem to vary but most are based on series expansions for the temperature, with the appropriate matching conditions. The most representative studies have been presented by Luikov [21] and by Pozzi and Lupo [22]. Essentially, the problem reduces to the determination of the unknown wall temperature distribution. The work of Luikov [21] is the only one which gives an expression for the two-dimensional temperature field in the fluid region. The corresponding solid temperature profiles are, as expected, for locations beyond a sufficient distance from the leading edge, linear. Pozzi and Lupo [22] on the other hand, present the wall temperature distribution in two parts, each arising from a different approximation, namely, the initial solution, for small dimensionless distances $\xi = x/b$ and the asymptotic solution for large ξ. In Fig. 2, the predicted wall temperature for grid dimensions of 171×57 is compared against the distribution obtained from the two analytical studies mentioned above, for a plate with $b = 5$ mm and the conductivity of wood, $\lambda_s = 0.17$ W/m K. The discrepancies that exist between the two analytical studies become obvious, however, the numerical results lie between the two analytical solutions. In the asymptotic regime the three curves come closer together, but the numerical solution and the solution of Luikov [21] are clearly shown to converge at approximately $x = 160$ mm, i.e., 32 plate thicknesses. The agreement in terms of vertical temperature profiles, both in the solid as well as in the fluid region is remarkably good (Fig. 2).

4. Results and discussion

4.1. Case 1 – labyrinth seal

Labyrinth seals are grooved structures on the surface of turbomachinery components, often combined with a honeycomb structure on the opposite surface, used to prevent leakage of gases along the flow path. The temperature control of the small clearances thus formed between the rotating and non-rotating parts is an essential part of the design process particularly of aircraft engines, due to the varying operating conditions during a flight cycle and the differential thermal expansion of the materials involved. The need to estimate the temperature field inside the seal material becomes therefore evident. Several studies have dealt with labyrinth seals, both by experimental and analytical methods and these were reviewed in a recent study by the authors [32]. The most representative ones were those by Wittig et al. [23,24], who studied both of the two main types of labyrinth seals, namely the 'straight-through' and the 'stepped' seals. The complete set of the experimental data of those has been included in the work of Jacobsen [25], while more details on their numerical scheme and additional computations have been presented by Schelling [26]. Other studies considered rotational effects, such as those by Sturgess and Datta [27] and Waschka et al. [28,29] and alternative computational approaches such as those by Rhode and Hibbs [30] and Rhode and Nail [31].

4.1.1. Present configuration

The present work is an additional contribution to the computational efforts mentioned above, by introducing the conjugate heat transfer effects, using boundary-fitted grids and employing a low-Reynolds number k–ϵ model which allows for better resolution and more accurate capturing of the flow details and heat transfer. The configuration selected here is a stepped-labyrinth seal based on the studies by Wittig et al. [23,24] and Jacobsen [25] and along with its characteristic dimensions is shown in Fig. 3. For the chosen configuration, numerical results were previously obtained by Schelling [26]. A

straight-through configuration has also been considered by the authors and published in a previous study [32], but here only the stepped seal was considered in order to compare with the experiments of Jacobsen [25] and to demonstrate the applicability of our conjugate approach on boundary-fitted grids, the need for which arises only in this case.

4.1.2. Computational aspects

The flow in labyrinth seals is characterized by strong accelerations in the slots between the fins and the opposite walls, which, depending on the ratio of total pressure upstream to static pressure at the exit, may lead to Mach numbers characteristic of compressible flow. Therefore, a compressible flow method was adopted in the present simulations and the pressure ratio p_o/p_{ex} was specified as a boundary condition, along with the inlet temperature and inlet turbulence quantities. The pressure-correction modification required for accounting for compressibility was incorporated according to the procedure proposed by Karki and Patankar [33], whereby a density correction ρ' is introduced and modeled by a first-order upwinding scheme. The equation of state for a perfect gas: $p' = \rho' RT$ is employed to provide the link between the pressure and the density corrections.

The conditions used are shown on Table 1. In all cases, the outermost horizontal walls are cooled and considered isothermal at T_w, while the inlet values are based on experimental conditions. The turbulence level

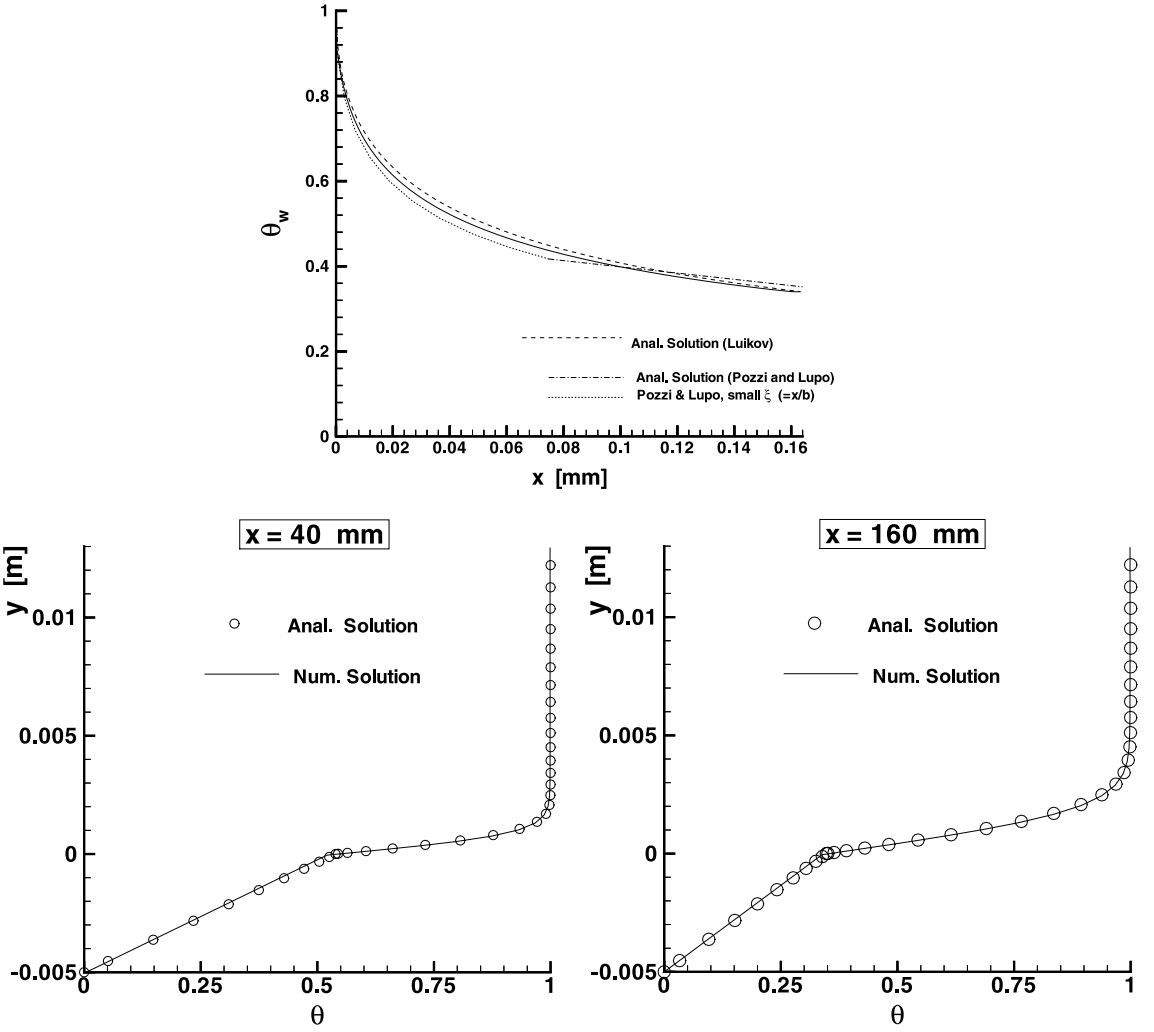

Fig. 2. Comparisons of predicted to analytical solutions for a flat plate 5 mm thick cooled from below. Top: Computed dimensionless wall temperature distribution (solid line) vs. the solutions of Luikov [21] and Pozzi and Lupo [22]. Bottom: Dimensionless temperature profiles vs. the solution of Luikov [21].

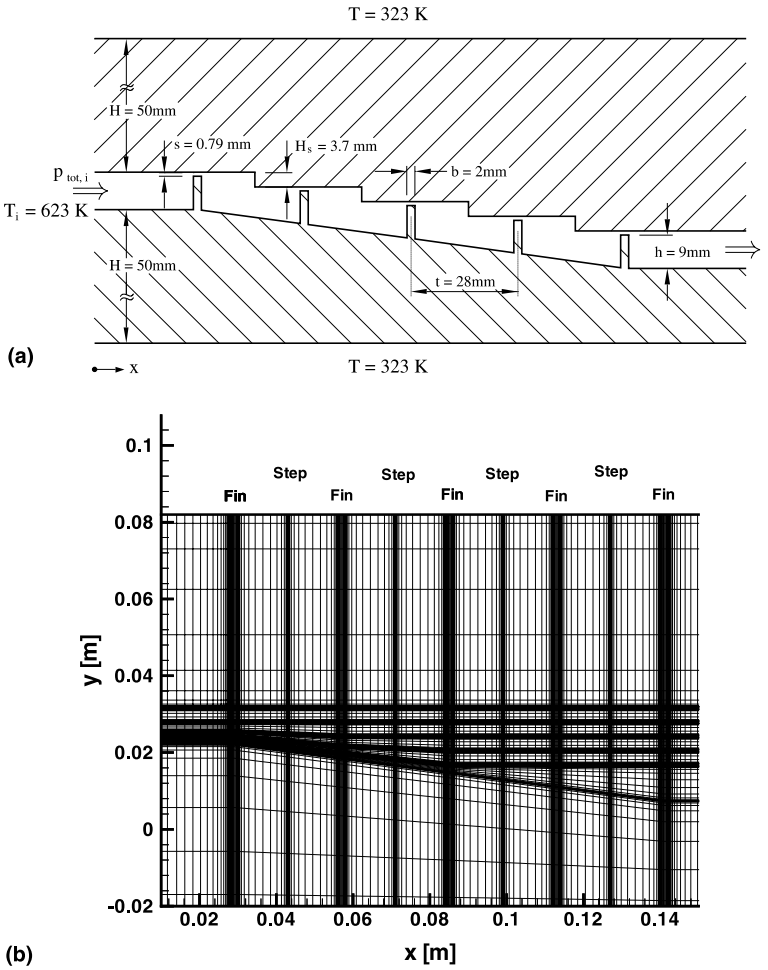

Fig. 3. Schematic of the stepped labyrinth-seal configuration with the corresponding significant dimensions (a) and section of the 300×158 computational grid (b).

at inlet is equal to 5% and the length scale is taken as 3% of the height of the inlet channel. As was demonstrated by some of the studies cited previously, there is a critical value of the parameter Ta/Re (where Ta is the Taylor number) below which a negligible effect of rotation on heat transfer is present. Therefore, additional terms due to rotation can be neglected in the mathematical model for our purposes, with the understanding that our analysis is valid within the appropriate range of Ta/Re.

According to Schelling [26], a downstream distance of 12 fin heights is necessary for properly placing the outflow boundary. This was also verified in the present computations whereas, for the inlet boundary, an upstream distance equal to one fin spacing was found sufficient. The critical region of the slots was resolved by 20–30 computational cells, which satisfied the condition $y^+ < 1$ at the nearest grid point to the wall. It should be noted that, to the authors' knowledge, this is the first study where a low-Reynolds form of the k–ϵ model is applied for predicting flows in labyrinth seals. Unlike the straight-through labyrinth, in the stepped-seal case each slot requires a different set of grid lines to run through it [32], therefore, the grid requirements for a good slot resolution increase proportionally to the number of fins. A grid with 300×158 nodes was eventually found necessary to meet the low-Reynolds model requirements and a section of it is shown in Fig. 3.

Table 1
Flow conditions and computed data for the labyrinth seal ($T_i = 623$ K, $T_w = 323$ K)

No.	p_o/p_{ex}	Re	C_D
1	1.08	2472	0.333
2	1.26	3837	0.347
3	1.45	4520	0.361

4.1.3. Flow and thermal fields

The flow and temperature fields are shown in Fig. 4 for $p_o/p_{ex} = 1.26$. No significant qualitative changes were observed for the different pressure ratios. A complex recirculating flow pattern develops, with two counter-rotating eddies in each cavity and smaller eddies at the foot of each fin, the one upstream of the first fin being the largest. This pattern is responsible for the significantly lower discharge coefficients (shown in Table 1) compared to the straight-through labyrinth (a factor of two or more) as found by Papanicolaou et al. [32], where the values are shown to increase slightly with the Reynolds number. The present predictions of C_D are in very good agreement with the experimental values for the same configuration given by Wittig et al. [23]. The peak axial velocity is located at the first two clearances with slightly lower values in the subsequent ones and the maximum Mach number is 0.27 for the highest pressure ratio considered, $p_o/p_{ex} = 1.45$. The temperature field in Fig. 4 shows the hottest spot in the solid to be the region between the first and the second fin, which is due to the fact that the velocities and therefore the heat transfer is higher in that region. The highest temperature gradients are also located in the first cavity. Inside the fins, the temperature contours are almost horizontal, with higher gradients in the vertical direction within the first two fins.

4.1.4. Wall temperatures and heat transfer

A better picture of the local temperature variations is provided by Fig. 5 where the numerical predictions are compared against the experimental results of Jacobsen [25]. The agreement varies between the different pressure ratios but, overall, it can be considered quite satisfactory. Better agreement is obtained for the highest two values, especially at $p_o/p_{ex} = 1.26$. In the plots of the wall temperatures the coordinate x^* shown on the abscissa varies along an unwound length of the entire fins, along with the bottom/top of the labyrinth chambers and the inlet–outlet channels. The stagnation points at the top upstream corner of each fin are clearly indicated by the sharp peaks in the numerical results (Fig. 5(a) and (b)), where the entire fin length in the clearance was resolved by 12 points, whereby in the measurements only one thermocouple was placed in the same area. As far as the gas temperature is concerned, a very good match between computed and measured values at inlet is found, with the discrepancies appearing further downstream, a tendency exhibited by the wall temperatures as well.

The heat transfer rates are evaluated here in terms of the mean Nusselt numbers, defined separately for the entire top surface (stator) and the entire bottom surface (rotor). These mean values are based on mean heat transfer coefficients $\bar{\alpha}$ defined as follows:

$$\bar{\alpha} = \frac{\dot{Q}_w}{A(\bar{T}_G - \bar{T}_w)}, \tag{13}$$

where $\dot{Q}_w$ is the total heat flux at either the entire top or bottom surface, obtained by a summation of the local heat fluxes, integrated over a local area. For the derivation of the mean temperatures and the appropriate reference temperatures and the heat transfer area A involved, the same convention as used in the measurements [24,25] was adopted, also described in detail in [32]. The mean Nusselt numbers are computed at each pressure ratio and are plotted against the corresponding Reynolds numbers in Fig. 5(d). The agreement with the experimental values is fairly good, both in terms of the

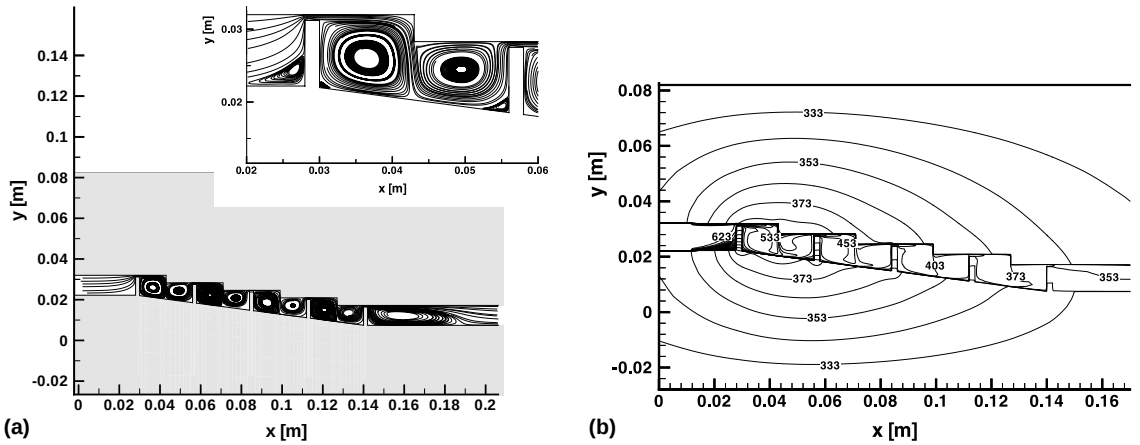

Fig. 4. Computed flow (a) and temperature field (bottom) for the labyrinth seal at $p_o/p_{ex} = 1.26$, $T_i = 623$ K, $T_w = 323$ K. (b) Flow details in the first chamber. Interval for isotherms: $\Delta T = 10$ K.

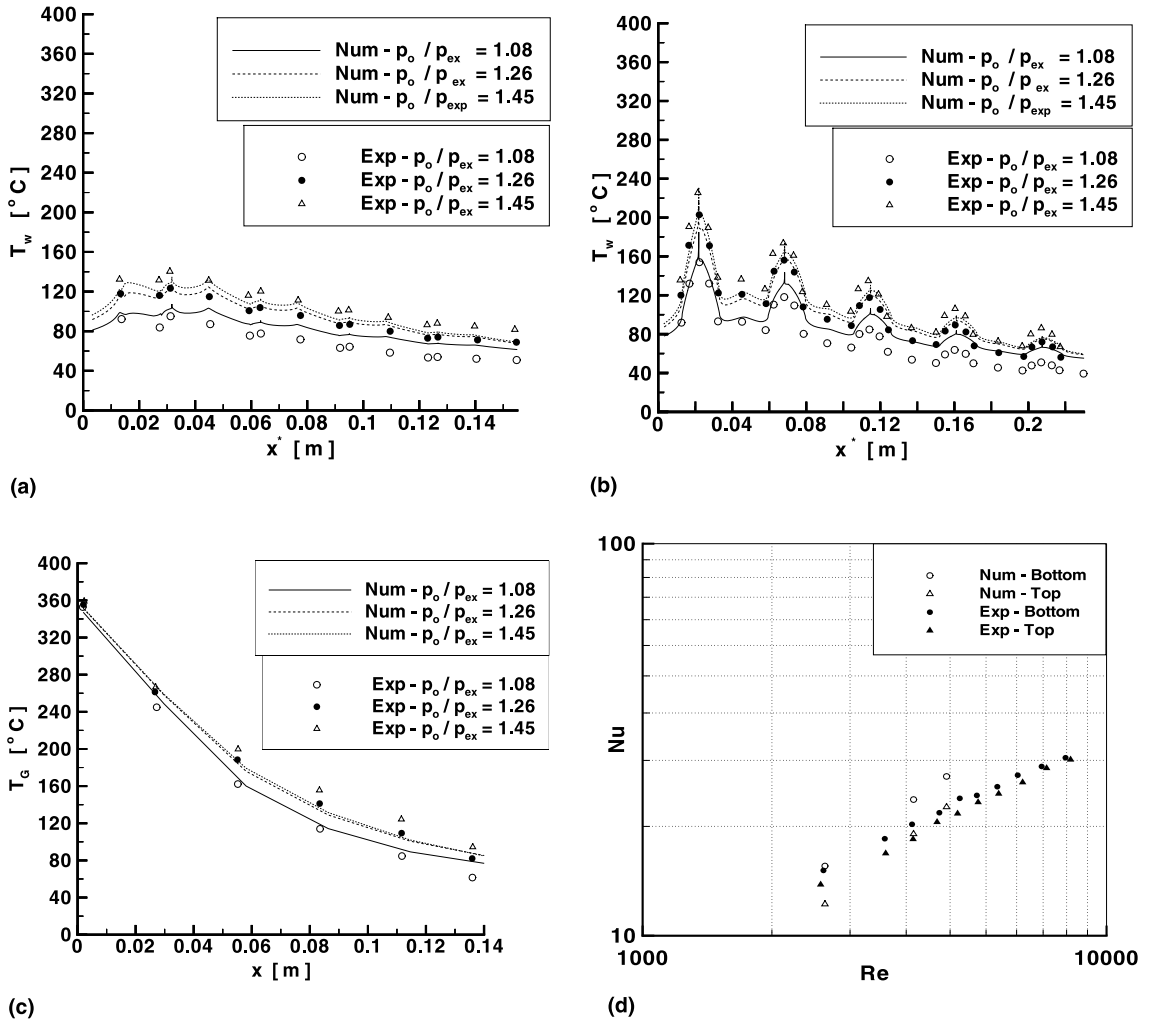

Fig. 5. Numerical vs. experimental temperature distributions at various pressure ratios and mean Nusselt vs. Reynolds number for the labyrinth seal. $T_i = 350°C$, $T_w = 50°C$. (a) Upper surface (stator), (b) lower surface (rotor), (c) gas temperature, (d) mean Nusselt number vs. *Re*.

slopes of the curves and the actual values, especially for the stator. The values for the rotor are slightly over-predicted. It is a general tendency that the rotor consistently exhibits higher heat transfer rates than the stator in the numerical results.

4.2. Case 2 – full-coverage film-cooling of combustor walls

4.2.1. Configuration and computational grid

Modern gas turbine combustors featuring high pressure and temperatures are subjected to very high thermal loads and can only be operated safely with intense cooling. However, advanced low-emission combustor technology requires most of the air to be fed through the fuel preparation system and reduction of the amount of liner cooling air is an important issue of modern designs. Therefore, efficient cooling techniques like effusion cooling, together with a detailed knowledge of the turbulent flow structure and heat transfer characteristic is of major importance in the design process. Besides the radiative heat transfer, convective heat transfer as well as heat conduction inside the combustor structure play an important role. As a representative test case, an effusion-cooled plate was selected which was experimentally investigated by Martiny et al. [34]. Details of both the experimental setup and the measurement techniques are available [34,35]. The geometry is shown in Fig. 6. A 12 mm thick flat plate with staggered rows of cylindrical holes inclined at an angle of 17° in the flow direction, is considered. The main supply of coolant comes from a

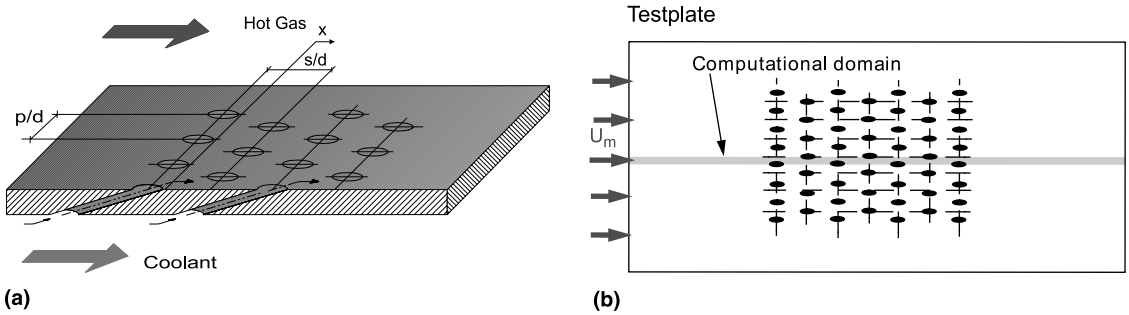

Fig. 6. Schematic of the effusion-cooled plate (a) and definition of the computational domain (b). The hole diameter is 4 mm and the pitches are $p = 8.96$ mm, $s = 29.84$ mm.

plenum at the bottom, which is bounded vertically by adiabatic walls. The extremely small angle together with a small hole pitch provides a large area for convective cooling inside the holes. Due to the repetitive hole pattern in the lateral direction, it is sufficient to consider a computational domain between the axis of two adjacent longitudinal rows of holes (Fig. 6). This domain includes a total of seven half holes.

In order to identify the conjugate heat transfer effects, the standard k–ϵ turbulence model with wall functions was used for the first computations. A H-type grid was used (Fig. 7). It includes mainstream channel, test plate, cooling holes and plenum. The grid consists of a total of 351 000 grid points (mainstream channel 132 000, test plate with cooling holes 130 000 and plenum 89 000 grid points). It should be noted, that it is possible here to use a single block grid, as the interior of the plate is also of importance for the heat transfer. Throughout the computational domain, the first grid nodes from the walls were placed in the fully turbulent region at an average dimensionless distance of $y^+ = 40$–90. It was found that by adding some curvature to the grid at the inlet of the holes and thus avoiding acute angles in this region, better convergence behavior is obtained. Curvature was not found to be very critical at the exit of the holes but, for the sake of a more symmetrical appearance, the same pattern was used. In the hole itself, the gridlines in the crossflow direction are gradually rotated to become perpendicular to the walls of the hole.

4.2.2. Boundary conditions and parameters

As inlet conditions for the main gas flow, the velocity profile was obtained from the experimental condition. The velocity attains a constant value of $u_m = 28$ m/s at a distance of 12 mm from the test plate bottom wall. In the plenum, vertical velocities are specified such that the resulting velocities in the injection holes yield the desired blowing ratio M. For the numerical calculations, both isothermal and non-isothermal conditions for the main flow and coolant temperature were specified in order to compare the predicted results with the measured velocity and temperature fields. For the heat transfer investigations, the inlet temperature of the main flow is prescribed from the experimental condition and increases in a power-law fashion from 475 K on the plate surface to a constant value of 550 K far from the plate. The coolant inlet temperature was set to 315 K, which yields a prescribed density ratio $D = \rho_c/\rho_m = 1.8$. It was not technically possible to use actual combustor temperatures in the experimental setup, therefore the real conditions were simulated by maintaining the same Reynolds number, blowing ratio and momentum ratio between the experiment and the actual case. The turbulence level was set to 4% at the inlet of the mainstream channel and 5% at the plenum entrance. The turbulent length scales are set to 0.03 of the inlet heights for both inflow boundaries. Detailed comparisons of numerical results with flowfield measurements of mean velocity are subsequently presented for two different blowing ratios and a density ratio of unity. Additionally, experimental data of film-cooling effectiveness and temperature profiles are compared for blowing ratios of $M = 0.5$, 1.2 and 3.0 and a density ratio of 1.8 for a plastic and a metallic test plate. For all results, the origin of the x coordinate is located at the trailing edge of the first row of the cooling holes (Fig. 8) and the y direction is normal to the plate.

4.2.3. Comparisons of flow fields

A comparison of the streamwise velocity profiles at different axial locations x/d along the centerline for blowing ratios of 0.5 and 3.0 are plotted in Fig. 8. For the lower blowing ratio of $M = 0.5$ good agreement is obtained for all axial locations $x/d \geqslant 15.9$. Slight differences between prediction and experiment are found at $x/d = 1$, downstream of the first row of holes. The experimental data show a significant momentum deficit at the wall which is not adequately captured by the prediction. The reason may be rooted to differences in the shape and contour of the jet in experiment and predic-

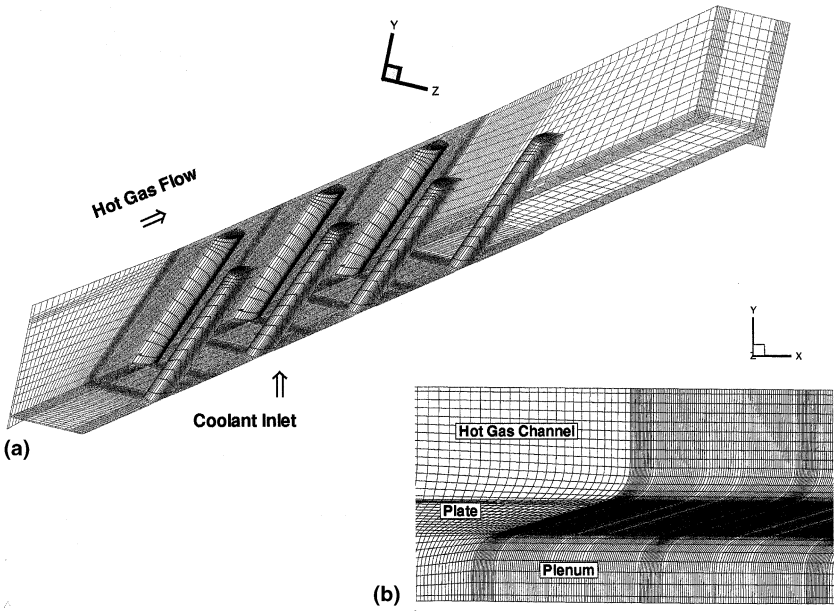

Fig. 7. Representative sections of the computational grid. (a) Panoramic view showing the discretization within the plate and the holes. (b) Vertical cross-section in the first two hole region. The height of the channel and the plenum are taken as 40 and 24 mm, respectively.

tion. While the calculation reveals a jet mainly concentrated along the centerline plane, the experiment indicates a jet outflow over a large portion of the hole outlet plane with lower velocities. A similar case was also analyzed by Giebert et al. [14], where film-cooling from scaled-up holes was investigated experimentally and numerically. That study revealed that the path and the shape of the exiting jet is strongly affected by the manner in which the coolant enters the injection hole, as well as by the correct prediction of the turbulence intensity. The fact that the turbulence production predicted by the present calculation at the inlet to the first row of holes is too low, combined with discrepancies in the jet velocity at that region, may well explain the observed deviations in the velocity profiles.

Fig. 8 also shows the same comparison for the blowing ratio of 3.0. For wall distances $y/d \geqslant 1.5$ the prediction agrees very well with the experimental data. However, for smaller wall distances $y/d < 1.5$ significant discrepancies are found which are due to deficits of the numerical calculation. The use of the wall function approach prohibits a fine resolution of the near wall boundary layer. Therefore, the jet lift-off which is observed in the experiment at that high blowing ratio, cannot be reproduced adequately in the calculation. Additionally, the standard k–ϵ turbulence model is well known [14,36] to underpredict the rate of the lateral spreading of the jets downstream of the hole. As a consequence, the interaction between adjacent jets is underestimated resulting in lower velocities near the wall. The thermal results are analyzed in terms of two basic quantities, the cooling effectiveness η and the normalized temperature Θ defined as:

$$\eta = \frac{T_m - T_w}{T_m - T_c}, \quad \Theta = \frac{T(y) - T_c}{T(y)_o - T_c} \tag{14}$$

T_w corresponds to the temperature at the hot gas channel wall, T_m is the temperature at the channel half-height, and T_c is the temperature of the coolant at the inlet. The temperature Θ is normalized by the temperature T_o at the inlet of the hot gas channel in order to eliminate its influence on the film cooling effect.

4.2.4. Effectiveness results for plastic plate

The upper part of Fig. 9 shows the contours of calculated overall film-cooling effectiveness for different blowing ratios over an effusion-cooled plate made of Tekapeek, a plastic material with low thermal conductivity ($\lambda = 0.33$ W/m K). The calculated thermal fields reveal the same trend in the temperature distributions with increasing blowing ratio as observed in the experimental investigation [35]. A non-homogenous temperature field is predicted, with a clearly distinguishable flow pattern of the cooling jets. Furthermore, it can be seen that an increase in the blowing ratio from $M = 0.5$ to $M = 1.2$ leads to higher values of the effectiveness downstream of the first three rows of holes, whereas a further increase up to $M = 3.0$ is accompanied by a reduction of the effectiveness, due to lift-off of the cooling

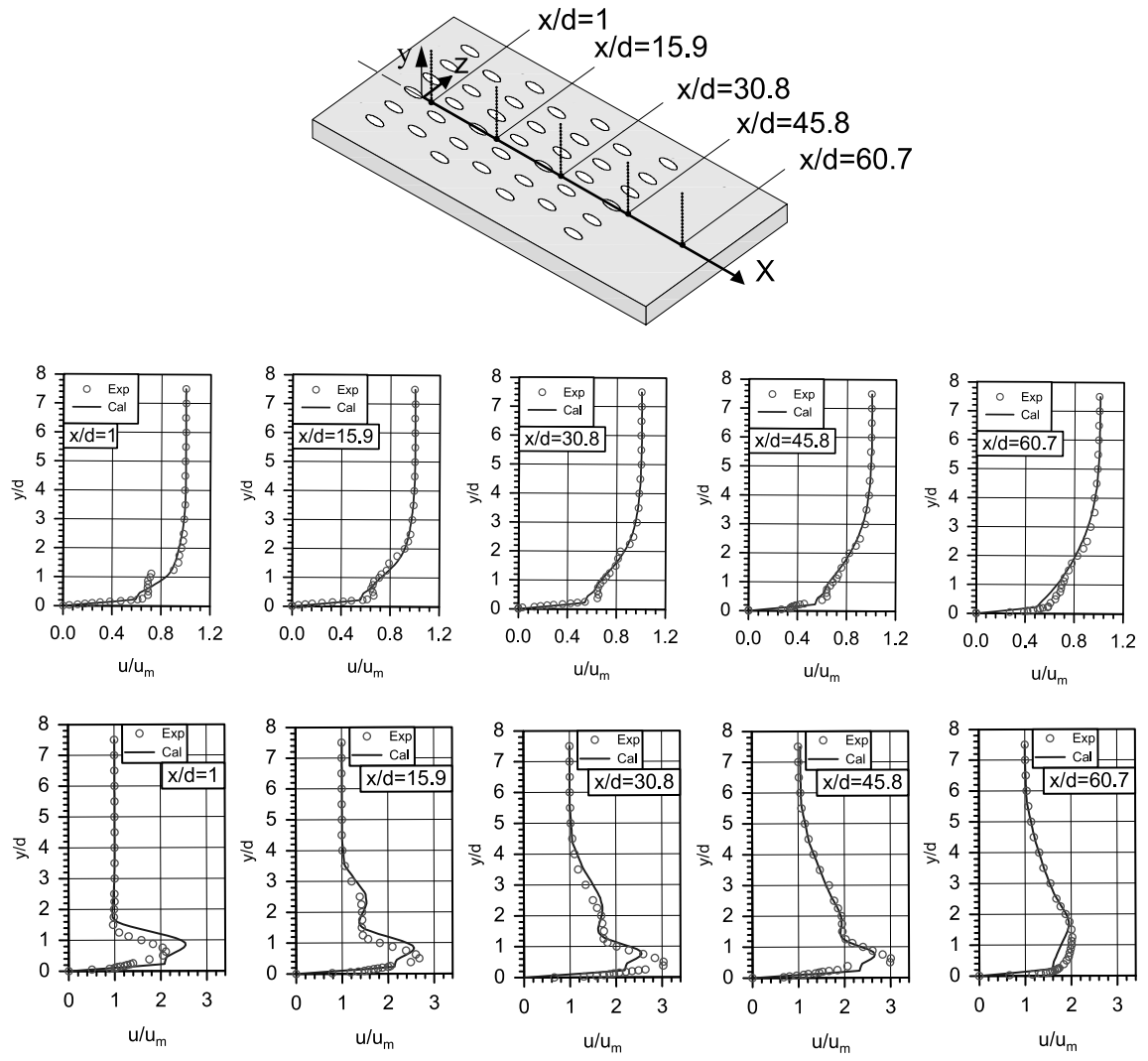

Fig. 8. Computed vs. experimental streamwise velocity profiles for blowing ratios of $M = 0.5$ (top row) and $M = 3.0$ (bottom row) at the measurement locations shown above.

jets. In the upstream region of the first row of holes, an increase of the effectiveness due to heat conduction inside the test plate is revealed for higher blowing ratios. However, since heat conduction is the sole mechanism of heat transfer, there is no optimum of the blowing ratio for which a maximum in the effectiveness can be obtained in that region. A better quantitative picture is obtained in Fig. 10 (top), where the laterally averaged effectiveness at different streamwise positions is compared.

For blowing ratios of $M = 0.5$ as well as $M = 1.2$ the agreement is quite good. Very good predictions are obtained for the maximum value of the effectiveness. However, its location slightly differs from the experimental data. For the highest blowing ratio ($M = 3.0$), the measured effectiveness shows a dip with a following increase in the streamwise direction. This effect is attributed to the detachment and subsequent reattachment of the jets. As mentioned previously, the lift-off of the jets cannot be adequately captured by the calculation because of the use of the wall functions. However, compared to the predicted results for the blowing ratio of $M = 1.2$, smaller values for the effectiveness are obtained indicating stronger penetration of hot gas flow underneath the jets.

4.2.5. Effectiveness results for metallic test plate

The calculated contours of overall film-cooling effectiveness for the same three blowing ratios and for a metallic test plate (*Incoloy* (800 H), $\lambda = 12.2$ W/m K) are shown at the bottom of Fig. 9. In contrast to the plastic

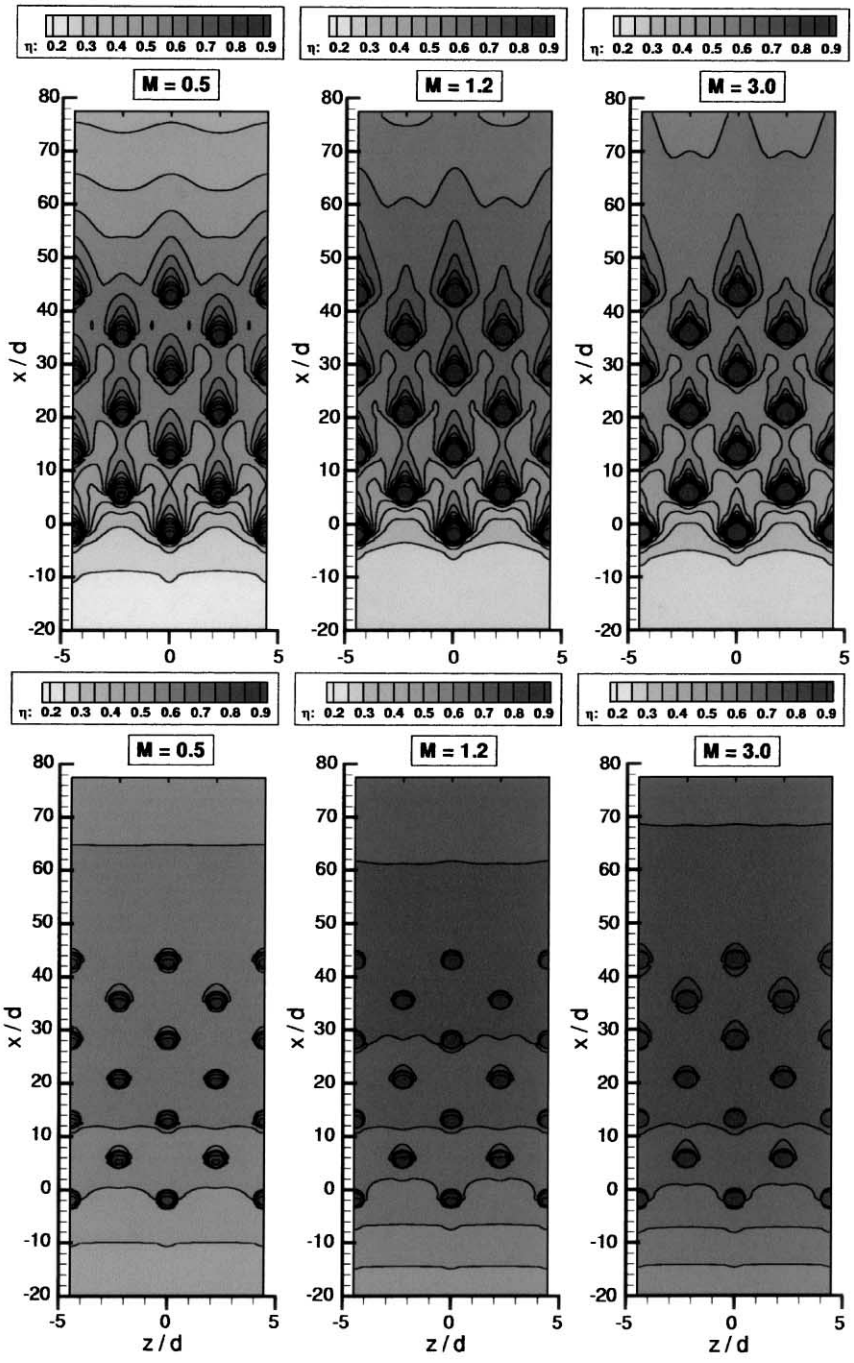

Fig. 9. Calculated film cooling effectiveness distribution for plastic plate (top) and metal plate (bottom) at various blowing ratios.

material, the predicted temperature distribution was found to be quite uniform at all blowing ratios, which is in good agreement to the experiment [35]. The experimental study also revealed that heat conduction inside the plate strongly affects cooling, in particular at higher blowing ratios. This effect is very well reflected by the prediction: due to the high thermal conductivity of the metallic plate, the flow pattern of the cooling jets cannot be identified. Moreover, a rise in the value of the blowing ratio is accompanied by a monotonic increase

of the film cooling effectiveness η, even at the highest blowing ratio. Unlike the situation for the plastic material, lower values of η are not found in the area of the first row of holes for $M = 3.0$ due to jet lift-off downstream the jet outlet. This phenomenon is completely compensated by the strong heat conduction inside the plate. Another less obvious effect is the intense cooling of the plate section upstream of the holes with increasing blowing ratio. Due to the higher thermal conductivity, this effect is more pronounced for the metallic test plate compared to the plastic material (Fig. 9, top).

The quantitative comparison of the laterally averaged effectiveness for the metallic test plate is shown at the bottom part of Fig. 10. Quite satisfactory results are obtained for η for downstream distances $x/d \leqslant 35$ at all blowing ratios even in the upstream portion of the first row of holes ($x/d < 0$). Further downstream ($x/d > 35$), significant discrepancies between calculation and experiment are found. The experimental data show a sharp decrease in η due to the missing conductive influence of the film cooling holes, whereas a moderate increase is found in the prediction with its maximum at $x/d \approx 60$. Those discrepancies are caused by an inadequate specification of the thermal wall boundary condition in the calculation. At the downstream end plane of the test plate a zero wall heat flux has been specified. However in the experiment, there was a non-negligible heat flux through the seal material between the end plane of the test plate and the surrounding containment. It should be noted, that for the plastic plate (Fig. 10, top) the specification of the zero flux thermal wall condition at the end plane has a minor effect due to the low thermal conductivity of the material.

4.2.6. Temperature profiles

Fig. 11 shows, as a typical result, the comparison of the normalized temperature profiles for a blowing ratio of $M = 1.2$ and the metallic test plate. The profiles correspond to the centerline locations along the streamwise direction. A remarkably good agreement between prediction and experiment was found for all locations x/d. Even the temperature profile in the near wall region $y/d < 0.5$, which indicates cooling of the test plate, is very well captured by the calculation. However, a closer inspection reveals that the measured temperature profiles show a strong variation whereas the calculation gives a linear distribution near the wall because of the use of the wall functions. It is well known [13], that in order to capture this variation of the temperature profiles near the wall, a low Reynolds number (LRN) extension of the turbulence model must be used, enabling a fine resolution of the near-wall region. As the two-dimensional problem of test case 1 of the present study has demonstrated, in which a highly complex flow was considered, quite promising results can be obtained when conjugate heat transfer phenomena are predicted by a low-Re turbulence model, albeit with an additional computational expense arising in three dimensions.

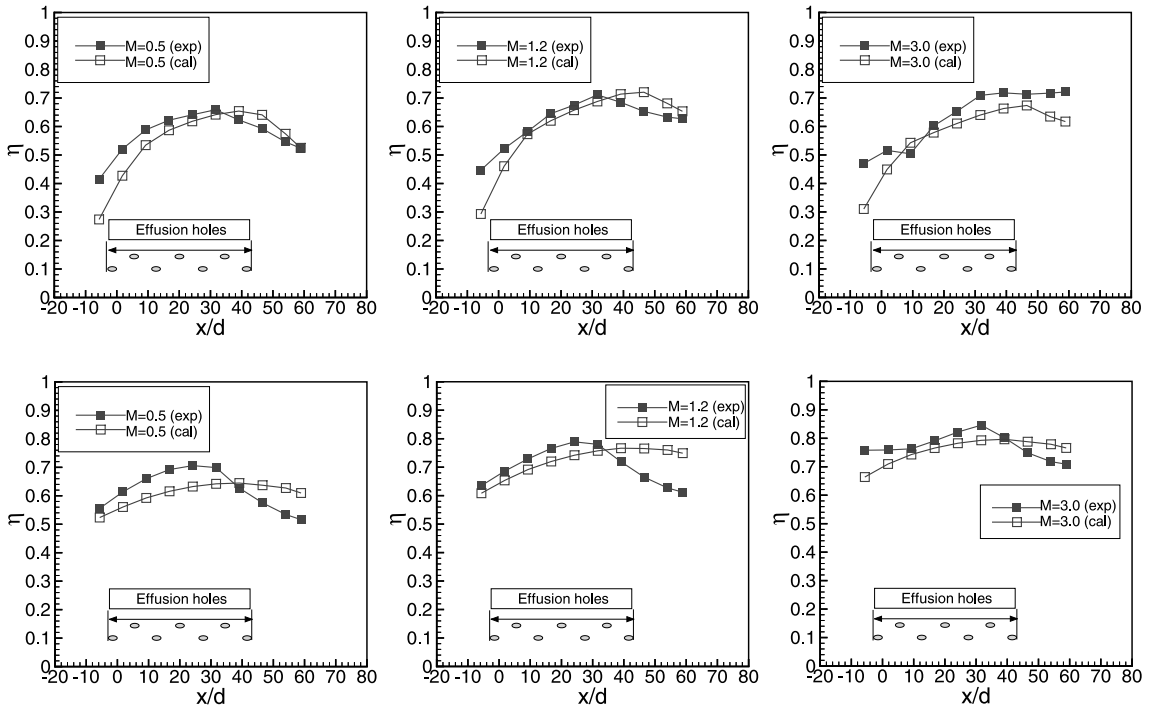

Fig. 10. Laterally averaged effectiveness for the plastic (top row) and the metallic test plates (bottom row) at various blowing ratios M.

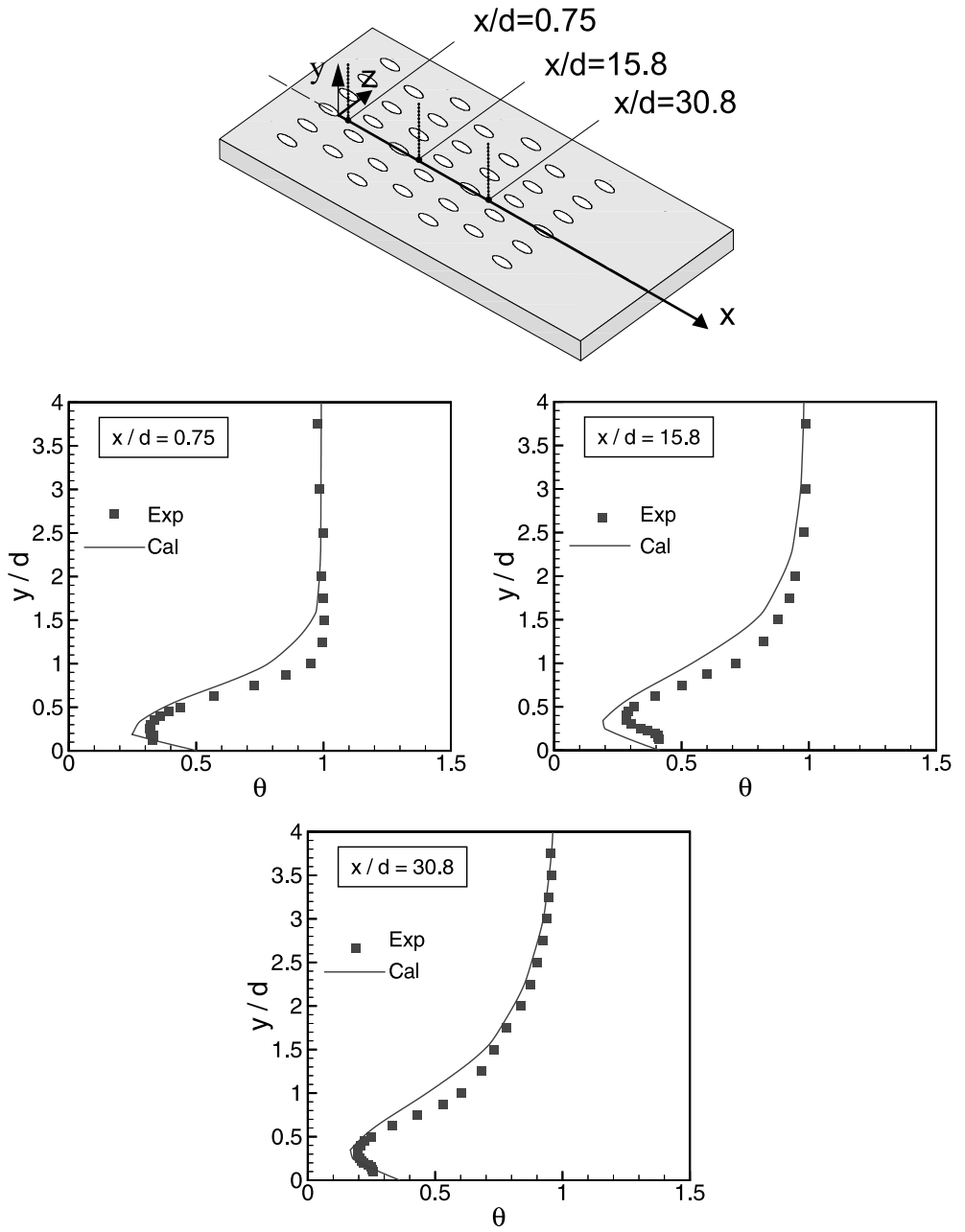

Fig. 11. Calculated and measured temperature profiles for $M = 1.2$ and the metallic test plate at the above shown locations.

5. Conclusions

A numerical procedure for simultaneous treatment of heat transfer in a fluid and heat conduction in a solid has been developed and tested. This approach extends the capabilities of an existing CFD code to conjugate heat transfer predictions. The methodology is consistent with the finite volume method, as it is based on conservation principles. Flat plate computations for conjugate heat transfer were compared with analytical results and demonstrated the successful handling of the conjugate boundary condition. The proposed method has been shown to be very useful for computations in typical flow problems from the field of turbomachinery where conduction heat transfer could be a decisive factor for a realistic prediction of temperature fields. For the example

of labyrinth seals, predicted surface temperature variations and heat transfer rates yielded a satisfactory agreement to the experimental data. The method has also been shown to capture the heat transfer phenomena of an effusion-cooled combustor liner where heat conduction inside the liner is of importance. The application of the wall function in the latter case was found to impose some restrictions, particularly in the capturing of both the lift-off of the cooling jets at high blowing ratios and the temperature variation in the near wall region. Switching to a low-Reynolds number extension of the turbulence model may overcome these deficiencies.

Acknowledgements

This work was supported through a grant by the Sonderforschungsbereich 167 "Hochbelastete Brennräume - stationäre Gleichdruckverbrennung", which is gratefully acknowledged by the authors.

Appendix A

The integrated, unknown enthalpy flux at face P on either side of the common interface of the two partial control volumes in Fig. 1 can be derived from Eq. (12) as:

$$I_{P,f} = A_w(h_P - h_W) - A_{n,f}(h_N - h_P) + A_{s,f}(h_P - h_S) - A_{t,f}(h_T - h_P) + A_{b,f}(h_P - h_B) + S_{h,f}, \quad (A.1)$$

$$I_{P,s} = A_e(h^*_E - h^*_P) + A_{n,s}(h^*_N - h^*_P) - A_{s,s}(h^*_P - h^*_S) + A_{t,s}(h^*_T - h^*_P) - A_{b,s}(h^*_P - h^*_B) - S_{h,s}(h^*), \quad (A.2)$$

where the As are the discretization coefficients [4], referring here to the surfaces of the split control volume. The two different values of enthalpy which are involved, h for the fluid and h^* for the solid, may be linearly related to each other at the interface when a constant value of C_P is assumed within each domain (and for the general case of a non-zero enthalpy of formation Δh_f), as follows: $h^* = r_C(h - \Delta h_f)$, where $r_C = C_{P,s}/C_{P,f}$. Thus, a single variable may be maintained at the end over the entire computational domain.

The flux continuity requirement at the interface is then enforced in an *integral sense:*

$$I_{P,f} = I_{P,s}. \quad (A.3)$$

By taking each of these two fluxes from Eqs. (A.1) and (A.2) and after rearranging, the following discretized expression is obtained for the interface nodes:

$$A^*_e(h_E - h_P) - A_w(h_P - h_W) + A^*_n(h_N - h_P) - A^*_s(h_P - h_S) + A^*_t(h_T - h_P) - A^*_b(h_P - h_B) = S_{h,f} + r_C S_{h,s},$$

where the discretization coefficients take the form: $A^*_e = r_C A_e$, $A^*_n = r_C A_{n,s} + A_{n,f}$, $A^*_s = r_C A_{s,s} + A_{s,f}$, $A^*_t = r_C A_{t,s} + A_{t,f}$, $A^*_b = r_C A_{b,s} + A_{b,f}$.

References

[1] D. Bohn, K. Kusterer, H. Schönenborn, 3D Numerical simulation of the flow through a turbine blade cascade with cooling injection at the leading edge, ASME Paper No. 96-GT-150, International Gas Turbine and Aeroengine Congress and Exhibition, Birmingham, UK, June 1996.

[2] E. Papanicolaou, Y. Jaluria, Mixed convection from a localized heat source in a cavity with conducting walls, Numer. Heat Transfer, Part A 23 (1993) 463–484.

[3] K.M. Kelkar, D. Choudhury, M. Ambrosi, Numerical method for the computation of conjugate heat transfer in nonorthogonal boundary-fitted coordinates, Numer. Heat Transfer, Part B 20 (1991) 25–40.

[4] S.V. Patankar, in: Numerical Heat Transfer and Fluid Flow, Hemisphere, Washington, DC, 1980.

[5] D. Bohn, B. Bonhoff, Berechnung der Kühl- und Störwirkung eines filmgekühlten, transsonisch durchströmten Turbinengitters mit diabaten Wänden, VDI-Bericht 1109, 1994.

[6] D. Bohn, H. Schönenborn, B. Bonhoff, H. Wilhelmi, Prediction of the film-cooling effectiveness in gas turbine blades using a numerical model for the coupled simulation of fluid flow and diabatic walls, in: F.S. Billig (Ed.), Proceedings of the 12th International Symposium on Air Breathing Engines, 1995, pp. 1150–1159.

[7] A. Heselhaus, D.T. Vogel, Numerical simulation of turbine blade cooling with respect to blade heat conduction and inlet temperature profiles, AIAA Paper No. 95-3041, 31st AIAA/ASME/SAE/ASEE Joint Propulsion, Conference and Exhibit, San Diego, CA, July, 1995.

[8] D. Bohn, N. Moritz, Influence of hole shaping of staggered multi-hole configurations on cooling film development, AIAA Paper 2000-2579, 34th Thermophysics Conference, Denver, CO, June, 2000.

[9] B.E. Launder, D. Spalding, The numerical computation of turbulent flows, Comput. Meth. Appl. Mech. Eng. 3 (1974) 269–289.

[10] J.H. Ferziger, M. Peric, in: Computational Methods for Fluid Dynamics, Springer, Berlin/Heidelberg, 1996.

[11] K. Abe, T. Kondoh, Y. Nagano, A new turbulence model for predicting fluid flow and heat transfer in separating and reattaching flows – I. Flow field calculations, Int. J. Heat Mass Transfer 37 (1994) 139–151.

[12] E. Benz, S. Wittig, A. Beek, L. Fottner, Analysis of cooling jets near the leading edge of turbine blades, in: 72nd Fluid Dynamics Panel Meeting and Symposium on Comp. and Exp. Assessment of Jets in Cross Flow, Winchester, UK, AGARD-CP-534, 1993.

[13] D. Giebert, R. Koch, A. Schulz, S. Wittig, Evaluation of advanced low-Reynolds number k–ϵ turbulence models for predicting convective heat transfer, in: Second International Conference in Turbulent Heat Transfer, Manchester, UK, 1998.

[14] D. Giebert, M. Gritsch, A. Schulz, S. Wittig, Film-cooling from holes with expanded exits: a comparison of compu-

tational results with experiments, ASME Paper 97-GT-163, 42nd Internaional Gas Turbine and Aeroengine Congress and Exhibition, Orlando, FL, June 1997.
[15] S.V. Patankar, D.B. Spalding, A calculation procedure for heat,mass and momentum transfer in three-dimensional parabolic flows, Int. J. Heat Mass Transfer 15 (1972) 1787–1806.
[16] C. Rhie, W.L. Chow, Numerical study of the turbulent flow past an airfoil with trailing edge, AIAA J. 21 (11) (1983) 1525–1532.
[17] B. Noll, Evaluation of a bounded high-resolution scheme for combustor flow computations, AIAA J. 30 (1) (1992) 64–69.
[18] B. Noll, S. Wittig, Genersalized conjugate gradient method for the efficient solution of three-dimensional fluid flow problems, Numer. Heat Transfer, Part B 20 (1991) 207–221.
[19] H. Stone, Iterative solution of implicit approximations of multidimensional partial differential equations, SIAM J. Numer. Anal. 5 (3) (1968) 530–558.
[20] H.A. Van der Vorst, Bi-CGSTAB: a fast and smoothly converging variant of Bi–Cg for the solution of nonsymmetric linear systems, SIAM J. Scient. Statist. Comput. 13 (2) (1992) 631–644.
[21] A.V. Luikov, Conjugate convective heat transfer problems, Int. J. Heat Mass Transfer 17 (1974) 257–265.
[22] A. Pozzi, M. Lupo, The coupling of conduction with forced convection over a flat plate, Int. J. Heat Mass Transfer 32 (7) (1989) 1207–1214.
[23] S. Wittig, U. Schelling, K. Jacobsen, S. Kim, Numerical predictions and measurements of discharge coefficients in labyrinth seals, ASME Paper 87-GT-188, ASME Gas Turbine Conference and Exhibition, Anaheim, CA, 1987.
[24] S. Wittig, K. Jacobsen, U. Schelling, S. Kim, Heat transfer in stepped labyrinth seals, ASME Paper 87-GT-92, ASME Gas Turbine Conference and Exhibition, Anaheim, California, 1987.
[25] K. Jacobsen, Experimentelle Untersuchungen zum Durchfluß und Wärmeübergang in Durchblick- und Stufenlabyrinthdichtungen, Ph.D. Thesis, University of Karlsruhe, Karlsruhe, Germany, 1987.
[26] U. Schelling, Numerische Berechnung kompressibler Strömungen mit Wärmeübergang in Labyrinthdichtungen, Ph.D Thesis, University of Karlsruhe, Karlsruhe, Germany, 1998.
[27] G.J. Sturgess, P. Datta, Application of CFD to gas turbine engine secondary flows – the labyrinth seal, Paper No. AIAA-88-3203, AIAA/ASME/SAE/ASEE 24th Joint Propulsion Conference, Boston, MA, 1988.
[28] W. Waschka, S. Wittig, S. Kim, Influence of high rotational speeds on the heat transfer and discharge coefficients in labyrinth seals, ASME J. Turbomach. 114 (1992) 462–468.
[29] W. Waschka, Th. Scherer, S. Kim, S. Wittig, Study of heat transfer and leakage in high rotating stepped labyrinth seals, in: Proceedings of the Fourth International Symposium on Transport Phenomena and Dynamics of Rotating Machinery, vol. A, Honolulu, Hawaii, 1992, pp. 326–335.
[30] D.L. Rhode, R.I. Hibbs, Tooth thickness effect on the performance of gas labyrinth seals, ASME J. Tribol. 114 (1992) 790–795.
[31] D.L. Rhode, G.H. Nail, Computation of cavity-by-cavity flow development in generic labyrinth seals, ASME J. Tribol. 114 (1992) 47–51.
[32] E. Papanicolaou, D. Giebert, R. Koch, A. Schulz, A discretization approach for conjugate heat transfer and application to turbomachinery flows, ASME HTD-Vol. 361-3/PID-Vol. 3, 1998.
[33] K.C. Karki, S.V. Patankar, Pressure based calculation procedure for viscous flows at all speeds in arbitrary configurations, AIAA J. 27 (9) (1989) 1167–1174.
[34] M. Martiny, A. Schulz, S. Wittig, Full-coverage film cooling investigations: adiabatic wall temperatures and flow visualization, ASME Paper 95- WA/GT-4, 1995.
[35] M. Martiny, R. Schiele, M. Gritsch, A. Schulz, S. Kim, High Efficient Cooling Concepts for Low Emission Combustors, Collaborative Research Center 167, High Intensity Combustors – Steady Isobaric Combustion, 1998.
[36] J. Leylek, R. Zerkle, Discrete-jet film cooling: a comparison of computational results with experiments, ASME J. Turbomach. 116 (1994) 358–368.